Effect of droplet deformation and internal circulation on drag coefficient

Yushu Lin* and John Palmore, Jr.†
Department of Mechanical Engineering, Virginia Tech, Blacksburg, Virginia, USA

(Received 30 June 2022; accepted 28 November 2022; published 21 December 2022)

This paper uses numerical approaches to investigate the effect of droplet deformation and internal circulation on droplet dynamics. Although droplet drag is a classical area of study, there are still theoretical gaps in understanding the motion of large droplets. In applications such as spray combustion, droplets of various sizes are generated and move with the flow. Large droplets tend to deform in the flow, and they have complex interactions with the flow because of this deformation. To better model spray, the physical understanding of droplets needs to be improved. Under spray conditions, droplets are subjected to a high-temperature-and-pressure environment, and the coupling between liquid and gas is enhanced. Therefore the deformation and internal circulation will affect the droplet drag coefficient more significantly than they would under atmospheric conditions. To study the mechanism of how droplet shape and internal circulation influence droplet dynamics, we have used direct numerical simulation (DNS) to simulate a droplet falling at its terminal velocity in high-pressure air. An in-house code developed for interface-capturing DNS of multiphase flows is employed for the simulation. The drag coefficient is calculated, and the results are consistent with the existing literature for slightly deformed droplets. The results show that the drag coefficient is directly related to the droplet deformation and droplet internal circulation. This paper also develops an analytical theory to account for the effect of the Weber number and fluid properties on droplet deformation.

DOI: 10.1103/PhysRevFluids.7.123602

I. INTRODUCTION

Many problems in science and engineering involve the formation and motion of droplets. Common examples include spray-painting, sneezing and disease prevention, fire suppression, and spray combustion. In these problems, accurately predicting how droplets move is important for predicting the efficacy of the engineering system. In this paper we are particularly interested in predicting the motion of large droplets in these problems, as there are gaps in the theory of the behavior of such droplets. Hence it is a topic worth further investigation.

The research motivation for this work is the phenomenon of spray combustion in aviation gas turbine engines. Spray combustion consists of a series of complex physical processes, including jet atomization (also called primary atomization), droplet breakup (also called secondary atomization), evaporation, droplet interaction, and combustion. In Fig. 1, a two-dimensional (2D) simulation is performed to show liquid jet atomization [1]. A liquid jet is injected into the cross flow, and droplets are produced from fragmentation of the jet. Although it is technically feasible to perform high-fidelity simulations of the type shown in Fig. 1, such simulations are largely restricted to use in specialized codes associated with academic and government research laboratories [1–3]. Simulating droplet motion with these codes is too computationally expensive in practice.

*linysh1997@vt.edu
†palmore@vt.edu

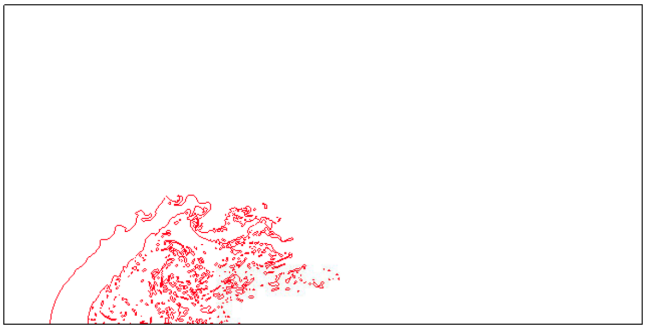

FIG. 1. 2D jet in a cross-flow simulation using the parameters of Ref. [2].

An alternative approach looks at reduced-order representations of droplets as Lagrangian particles. The common starting assumption for the Lagrangian model is that droplets are perfectly spherical and have no internal flow. This is accurate for the smallest spray droplets; however, in spray, droplets come in a range of sizes. The largest ones are large enough to see significant deformation, which can fundamentally affect their behavior including drag [4] and evaporation rate [5,6]. Therefore we need to improve the physical understanding of droplets to better predict the dynamics of droplets represented by Lagrangian particles. More specifically, in this paper we perform a study of how the droplet drag coefficient is dependent on relevant parameters. However, we do not do a wide parameter sweep of all scenarios possible. Instead, we focus on understanding the physical mechanisms that govern droplet drag and look at several extreme conditions which succinctly demonstrate these principles.

The study of the droplet drag coefficient has received attention from researchers for decades. The simplest approximation is to use the standard drag curve of rigid spheres as derived by Stokes. Several empirical correlations have been posed by multiplying a correction factor to Stokes' law, $C_d = 24/\mathrm{Re}$, where Re is the Reynolds number. A review of these correlations can be found in Ref. [7]. For viscous liquid spheres, the droplet internal flow was assumed to be Hill's spherical vortex in Ref. [8], while the gaseous flow was a potential flow. Based on these approximations, by integrating the surface stress, an analytical drag coefficient correlation of the first-order approximation was derived depending on Re and dynamic viscosity ratio $\mu^* = \mu_l/\mu_g$ in Ref. [8]. The subscript l and g represent liquid and gas, respectively. For Re up to 200 with arbitrary μ^*, the C_d correlation for viscous spherical droplets was found from numerical simulations in Ref. [9], where the flow was considered steady and axisymmetric, and the Navier-Stokes equations were solved by solving the stream function and vorticity equation in spherical coordinates. In Ref. [10], a numerical method was developed by introducing a two-layer concept to capture the very thin boundary layer at the liquid-gas interface, and a drag coefficient for viscous spherical droplets was well established for intermediate $\mu^* = \mu_l/\mu_g$. In Ref. [4], drag correlations for deformed droplets were found by examining and fitting experimental results in Ref. [11]. For drag coefficient correlations of deformed droplets, one can refer to Ref. [12]. In Ref. [12], a finite-volume method was used in a nonorthogonal adaptive grid system, and the energy equation was solved as well for droplet evaporation. To investigate the effect of droplet internal circulation, it was revealed in Ref. [13] by scaling analysis that the multiplication of the density ratio $\rho^* = \rho_l/\rho_g$ and the dynamic viscosity ratio $\Lambda = \sqrt{\rho^*\mu^*}$ characterizes the coupling between the liquid and gas phases. However, Ref. [13] refers to a spherical droplet. Helenbrook and Edwards [14] and Feng [15] investigated both the effect of deformation of droplets and the effect of internal circulation of droplets. An arbitrary-Lagrangian-Eulerian mesh movement scheme with unstructured mesh was used in Ref. [14] to resolve the position of the phase interface. In Ref. [15], it was found that given Re and Weber number We, the droplet drag coefficient was dependent only on $\rho^*/(\mu^*)^2$, which was equivalent to the Ohnesorge number Oh in such a case. The Navier-Stokes equations were

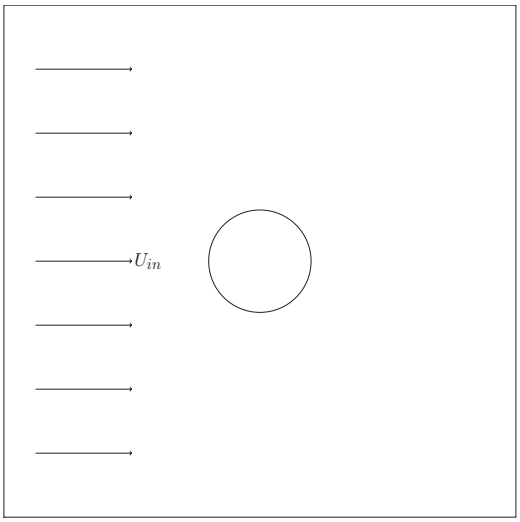

FIG. 2. 2D slice of the computation domain.

solved by the Galerkin finite-element method in cylindrical coordinates. The aforementioned works focus on steady droplets. For a spherical droplet that is accelerating or decelerating in the gas, in Refs. [16,17], a correlation to C_d was found based on conical-driver shock tube experiment results, and it was dependent on a nondimensional relative-acceleration parameter. For deformed transient droplets, the C_d correlation can be found in Ref. [18], where ANSYS FLUENT was used to solve the Navier-Stokes equations.

For gas turbine combustion, classical droplet models are incomplete, because in a high-temperature-and-pressure environment, droplets are usually highly deformed, and the coupling between gas and liquid phases is enhanced. These phenomena result in different behaviors between droplets in spray and the droplet theory; consequently, a detailed study of both the effect of droplet shape and the effect of internal circulation will be needed. To study their effect on the droplet drag coefficient, we utilize an in-house code developed by our group [19] for interface-capturing direct numerical simulation (DNS) of vaporization multiphase flows. The code uses the volume-of-fluid (VOF) method to determine the location of the phase interface and solves Navier-Stokes equations in the whole domain in Cartesian coordinates. Transient droplet motion can be calculated by the code directly. A result in this paper is that a more accurate drag coefficient calculation is found by correcting the droplet frontal area estimation, which agrees with some of the previous literature. It is noteworthy that the 3D code simulates droplet shape deformation from first principles without any assumptions, and it also includes the effect of pressurized gas on the internal circulation of droplets. More details about the numerical implementations can be found in Sec. III.

II. PROBLEM FORMULATION

We simulate droplet deformation in a uniform convective flow in 3D. An initially spherical *n*-decane droplet with diameter D is centered in a cubic computation domain with size $(8D)^3$. A flow of dry air enters the domain uniformly at a speed of U_{in} from the inlet boundary and leaves the domain freely at the exit boundary; see Fig. 2. Periodic boundary conditions are applied to other sides of the domain boundaries. We choose the droplet center of mass as the frame of reference, such that the droplet will be stationary at the center of the domain. To achieve this, an artificial gravity will be used to balance the drag force, and the droplet will reach its terminal velocity. The artificial gravity will be discussed in more detail in Sec. III D.

TABLE I. Properties of the gas and liquid.

Cases	ρ^*	$P^* = P/P_{\text{atm}}$	We
a1, a2, a3, and a4	20	38.2	1, 3, 6, and 9, respectively
b1, b2, b3,	20, 40, 60, 160,	38.2, 19.1, 9.56,	6
b4, and b5	and 765, respectively	4.78, and 1.0, respectively	

A. Controlling parameters

Based on Refs. [13,20], the following nondimensional groups are determined to be the controlling parameters in our problem:

$$\text{Re} = \frac{\rho_g U_{in} D}{\mu_g}, \tag{1}$$

$$\text{We} = \frac{\rho_g U_{in}^2 D}{\sigma}, \tag{2}$$

$$\Lambda = \sqrt{\frac{\rho_l \mu_l}{\rho_g \mu_g}}. \tag{3}$$

The Reynolds number compares the inertial force and viscous force of gas flowing past the droplet. The Weber number compares the inertia of the gas and the surface tension of the liquid, indicating how well a droplet can keep itself spherical. Λ reveals the strength of internal motion of the droplet compared with the freestream gas flow. In a real flow, Λ will vary due to the changes in temperature and pressure of the liquid and gas. Comparing atmospheric conditions with those in a gas turbine engine, the dominant effect in Λ is due to gas density change accompanying the high gas pressurization. With a fixed Reynolds number, we can control the droplet shape by changing the Weber number or control the internal flow by changing the liquid-density-to-gas-density ratio.

B. Configurations

We perform various numerical simulations of a droplet falling at its terminal velocity at $\text{Re} = 70$. To study its deformation and internal circulation, we must ensure that the droplet does not break up. In all our cases, the Ohnesorge number Oh is less then 0.1, so that the droplet will not break up for $\text{We} < \text{We}_{\text{critical}} \approx 12$ [21]. The simulation parameters for the setup are listed in Table I. The dynamic viscosity is $2.474\,25 \times 10^{-5}$ kg m^{-1} s^{-1} for gas at the liquid-gas interface temperature, which is the boiling temperature of *n*-decane at around 447.3 K [22], and 2.0241×10^{-4} kg m^{-1} s^{-1} [23] for liquid. The density of liquid is 603.87 kg/m^3 [23], and the density of gas is determined by the density ratio. The surface tension is set to be 0.010 24 kg/s^2 [23]. The properties of the liquid depend weakly on the pressure, so we treat liquid properties as constants. The droplet diameter is determined to achieve the parameter sets in Table I, and the domain size is chosen in proportion to the diameter.

III. NUMERICAL METHODS

We employ an in-house code called NGA [24] to simulate the droplet falling at its terminal velocity. NGA was developed for solving low-Mach-number turbulent flows and was further developed for interface-capturing multiphase flows by Palmore and Desjardins [19]. This section will give a brief overview of some of the algorithms.

A. Governing equations

The governing equations for conservation of momentum in both liquid and gas phases are

$$\frac{\partial(\rho \boldsymbol{u})}{\partial t} + \nabla \cdot (\rho \boldsymbol{u} \otimes \boldsymbol{u}) = -\nabla p + \nabla \cdot \mu \boldsymbol{S} + \boldsymbol{f}, \tag{4}$$

where $\boldsymbol{S} = \nabla \boldsymbol{u} + \nabla \boldsymbol{u}^{\top} - \frac{2}{3}\nabla \cdot \boldsymbol{u}$ and $\boldsymbol{f}$ is the external body force used for stabilizing the droplet at the center. The conservation of mass is guaranteed by solving the pressure term from pressure Poisson equations. The pressure Poisson equation is solved by using the ghost fluid method (GFM) [25]. In Eq. (4), ρ and μ are the effective density and effective viscosity introduced in Sec. III B for solving governing equations in the one-phase approach.

B. Interface-capturing method

To solve the liquid-gas interface, the VOF method is employed. In the VOF method, the volume fraction ϕ is defined in each cell as the volume fraction occupied by the liquid. For cells entirely within the liquid phase, $\phi = 1$, and for cells within the gas phase, $\phi = 0$. When the phase interface crosses a cell, the volume fraction will be within the range of (0, 1), and the effective density and viscosity in these cells can be defined as

$$\rho = \rho_l \phi + \rho_g (1 - \phi), \quad \mu = \mu_l \phi + \mu_g (1 - \phi). \tag{5}$$

The effective density and viscosity are used to solve the governing equations of the gas and liquid in a one-phase approach [19]. In this way, the velocity fields of the gas and liquid are treated as a union, and the governing equations can be solved only once for one unified velocity field. The evolution of the volume fraction scalar field is governed by the following advection equation with the velocity field being the gas-liquid union velocity field [26]:

$$\frac{\partial \phi}{\partial t} + \boldsymbol{u} \cdot \nabla \phi = 0. \tag{6}$$

C. Jump conditions across the interface

To ensure the conservation of mass and momentum at the phase interface, several matching conditions at the phase interface should be satisfied. The current simulations are for nonevaporating droplets, so the only jump condition is the pressure jump due to surface tension:

$$P_g - P_l = -\sigma \kappa, \tag{7}$$

where σ is the liquid surface tension and κ is the curvature of the droplet surface and is defined so that $\kappa > 0$ for convexly shaped liquid regions.

D. Artificial gravity

The droplet in the computational domain will move due to the drag force. With the desire of studying a stationary droplet, Palmore and Desjardins [27] devised a method that mimics the flow over a falling droplet at terminal velocity. In this method, the gravity is fixed and the terminal velocity is converged. However, due to the uncertainty of the drag coefficient caused by droplet deformation, the velocity reached will still be lower than the terminal velocity. To ensure that a constant terminal velocity was reached, Lin *et al.* [28] (also see Ref. [29]) developed a gravity update scheme to balance the changing drag force. Since the drag force is unknown explicitly, their method is based on a feedback control loop:

$$g^{n+1} = g^n + k_U U_d + k_X X_d, \tag{8}$$

where U_d is the droplet velocity and X_d is the droplet center-of-mass position in the x direction. k_U and k_X are gains of U_d and X_d, respectively. This approach has higher robustness under inflow

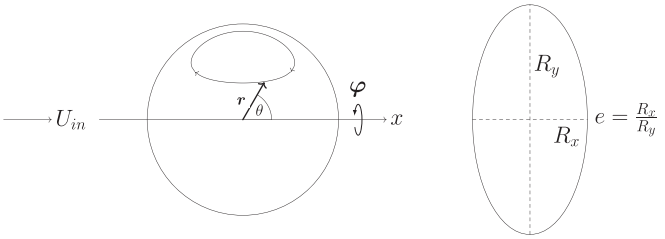

FIG. 3. Coordinate system of spherical and deformed droplets.

boundary conditions compared with Ref. [27]. For the current setting, we set $k_U = 1/(2\tau_c)$ and $K_X = 0$, where τ_c is the capillary time defined as $\tau_c = \sqrt{\frac{\rho_l+\rho_g}{\sigma}}(\frac{D}{2\pi})^{\frac{3}{2}}$.

E. Quantification of internal circulation

Because the increase in pressure in the gas turbine can be significant, the gas density will increase proportionally through the ideal gas law. In contrast, the liquid density remains almost constant regardless of the pressure change. Hence the gas density change represents the physical process of the pressure change. In addition, studies such as those in Refs. [13,15,28] have revealed that internal circulation is dependent on the density ratio. Therefore we choose the gas density to be the controlling parameter for changing the strength of internal circulation. To quantify the strength of internal circulation, several common physical quantities are considered, including the maximum liquid velocity, the maximum and mean vorticity of the droplet, and the droplet enstrophy. Based on our previous work, maximum velocity and vorticity are not good choices due to their sensitivity to numerical errors, while volume-averaged variables are better in representing the internal circulation strength [28]. Thus we only use volume-averaged variables in this paper. The definitions of vorticity $\boldsymbol{\omega}$ and enstrophy $\mathcal{E}$ are

$$\boldsymbol{\omega} = \nabla \times \boldsymbol{U}_L, \tag{9}$$

$$\mathcal{E} = \tfrac{1}{2}\boldsymbol{\omega}^2, \tag{10}$$

where U_L is the liquid phase velocity field, ω is vorticity, and $\mathcal{E}$ is enstrophy. In addition, a variable we have termed the Hill's constant is also used as a measure of the internal circulation strength. The Hill's spherical vortex [30] is the simplest modeling of the droplet internal circulation, and the Hill's constant is a quantity derived from the Hill's solution to represent the internal circulation strength. The vorticity magnitude of the Hill's vortex is given by Batchelor [31]:

$$|\boldsymbol{\omega}| = A r_\perp \quad , \tag{11}$$

where $\boldsymbol{r}$ is a vector within the droplet from the droplet center (θ is the angle enclosed by $\boldsymbol{r}$ and the x axis, $r_\perp = |\boldsymbol{r}| \sin\theta$) and A is the Hill's constant representing the vortex strength. In our code, the local Hill's constant is calculated by using the following expression:

$$A = \frac{\boldsymbol{\omega} \cdot \hat{\boldsymbol{\varphi}}}{r_\perp}, \tag{12}$$

where $\hat{\boldsymbol{\varphi}}$ is the unit vector normal to $\boldsymbol{r}$ in the $\boldsymbol{\varphi}$ direction; see Fig. 3.

When calculating the mean vorticity, enstrophy, and Hill's constant, we will implement a volume integration over the droplet:

$$\bar{\psi} = \frac{1}{V} \iiint_V \psi \, d\forall, \tag{13}$$

where V is the volume of the droplet, ψ is any variable that needs to be volume averaged, and $\bar{\psi}$ is the volume-averaged variable.

A limitation of the numerical strategy for the momentum solution is that the liquid velocity and gas velocity are solved on one field. For cells near the phase interface, a large velocity difference might occur if gas velocity is included. To avoid including gas velocity in the calculation of circulation variables, the liquid phase velocity field U_L is computed as a postprocessing step at each time step from the combined velocity. This value is smoothly extrapolated into the gas value using the technique of Ref. [32], and the smoothed field is the one used for the computations of the vorticity, enstrophy, and Hill's constant.

F. Calculation of the drag coefficient

Assume that the droplet is stationary in the domain and the droplet motion is dominated in the x direction; then the drag coefficient C_d can be computed by balancing the drag force and gravity:

$$\tfrac{1}{2}C_d\rho_g U_{in}^2 A_p = (\rho_l - \rho_g)gV, \tag{14}$$

where A_p is the projected droplet frontal area calculated by using the effective radius r_{eff}. r_{eff} is the radius of a spherical droplet which has the same volume as the deformed droplet. Since we are not working on evaporation in this paper, droplet volume and r_{eff} will not change, and thus A_p is a constant.

Some further modifications can be made on the drag coefficient estimation. At first approximation, we can assume that the deformed droplet is spheroid [4] and use the aspect ratio e of the spheroidal droplet to calculate A_p more accurately. In this paper, we define e as the ratio of the semiaxis lengths in the x and y directions, i.e., $e = R_x/R_y$; see Fig. 3. In the code, we estimate the semiaxis length by choosing the maximum of the summation of the volume fraction at each line along the direction. Secondly, if the droplet is stationary at the center of the domain as expected, the terminal velocity will be equal to the inlet gaseous velocity. However, after experiencing the initial transient period, often the droplet will move very slowly at a nearly constant speed even with the gravity update scheme discussed in Sec. III D. This cannot be avoided since motion by a constant velocity satisfies the Navier-Stokes equations via its Galilean invariant property. To account for this, we can replace U_{in}^2 by $(U_{in} - U_d)^2$ to improve the accuracy of terminal velocity estimation. Here, U_d is the droplet average value of the x component of U_L. Strictly, Eq. (14) requires the droplet to be nonaccelerating. To quantify the effect of the small-droplet acceleration, we also include the acceleration term in the calculation of the droplet coefficient:

$$\tfrac{1}{2}C_d\rho_g(U_{in} - U_d)^2 A_p = (\rho_l - \rho_g)gV + \rho_l aV. \tag{15}$$

An advantage of this approach is that there could be other terms affecting droplet drag other than gravity. For example, in Refs. [33,34], it is mentioned that the added mass term and history term can play a role in certain circumstances. These terms are usually negligible in steady-state problems; however, they may be important for the initial transient portion of the flow. Since the acceleration is calculated directly from the droplet motion, the acceleration term automatically captures all effects that are not explicitly given in Eq. (14). Therefore the effects of the added mass term and history term are implicitly included in the acceleration term.

To find an accurate calculation of acceleration a, we have tried three different ways to compute it. We label them as a_1, a_2, and a_3: $a_1 = dU_d/dt$, $a_2 = d^2X_d/dt^2$, and $a_3 = d(U_d^2)/2dX_d$. X_d is the centroid of the droplet. The three potential definitions were chosen to control the numerical error of the approximation used to compute the acceleration. a_1 is the most straightforward definition of the acceleration. However, previous simulations have shown that this may not be a perfect representation of droplet motion, because U_d does not exactly represent the motion of the droplet centroid due to errors in the extrapolation process used to define U_L. a_2 computes the acceleration directly from the droplet position but is a slightly more noisy value. For example, a pinned droplet that oscillates in place will demonstrate changes in a_2 due to slight asymmetries in the interface

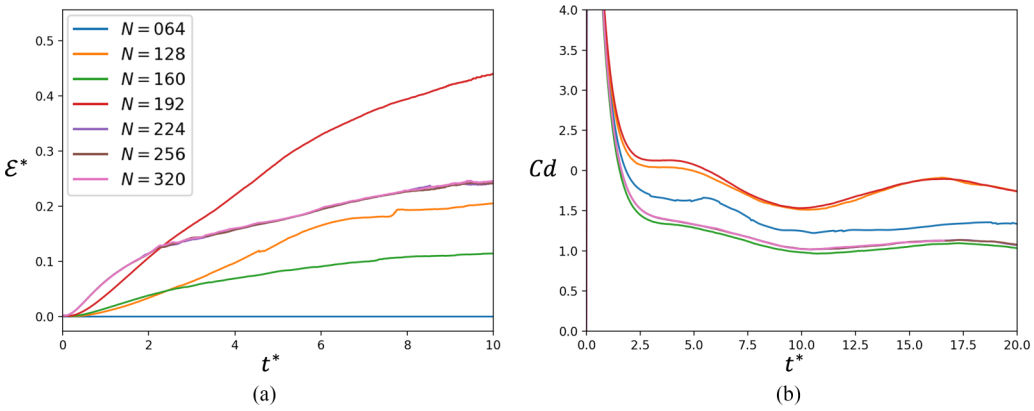

FIG. 4. Enstrophy and drag coefficient on different grids. (a) Nondimensionalized volume-averaged enstrophy (the definition of nondimensionalization is given in the caption of Fig. 12). (b) Drag coefficient calculated using Eq. (14) with A_p estimated using r_{eff}.

shape. a_3 is borrowed from 1D kinematics of particles. Since it combines U_d and X_d, it has the potential to control for errors in either of the other definitions. The discretized form of each is

$$a_1^n = \frac{U_d^{n+1} - U_d^{n-1}}{2\Delta t}, \tag{16}$$

$$a_2^n = \frac{X_d^{n+1} - 2X_d^n + X_d^{n-1}}{\Delta t^2}, \tag{17}$$

$$a_3^n = \frac{\left(U_d^{n+1}\right)^2 - \left(U_d^{n-1}\right)^2}{2\left(X_d^{n+1} - X_d^{n-1}\right)}, \tag{18}$$

where the superscript n denotes the nth time step.

IV. RESULTS AND DISCUSSION

In this section, based on parameters explored in Sec. II B, we will discuss the results of our simulations to see how the liquid-density-to-gas-density ratio and Weber number affect droplet deformation and the drag coefficient.

A. Grid convergence study

It will require a very fine mesh to resolve the liquid-gas interface and internal flow inside the droplet. Therefore, to eliminate the influence of grid resolution, we will first perform simulations with different grids to determine a suitable mesh resolution. The flow conditions selected for grid convergence study are $\text{We} = 1$, $\text{Re} = 70$, and $\rho^* = 20$. In this case, since the droplet is nearly spherical, the droplet internal circulation will not be further affected by droplet deformation, so the mesh size will be the only factor that influences internal flow. We increase grid points from $N = 64$ to $N = 320$ on each dimension and examine the results of the drag coefficient and enstrophy of the droplet; see Fig. 4. For very coarse meshes, the results vary significantly; however, the results finally converge at $N = 224$, 256, and 320, i.e., the drag coefficient and enstrophy will not change anymore with increasing grid points for $N > 224$. Therefore we finally chose $N = 256$ for our simulations.

It is interesting to note that the results shown in Fig. 4 do not demonstrate a monotonic trend as the mesh resolution increases. To explain this, we further examined the internal structure of the droplet. In Fig. 5, the vorticity in the z direction is plotted. The complex interaction between the

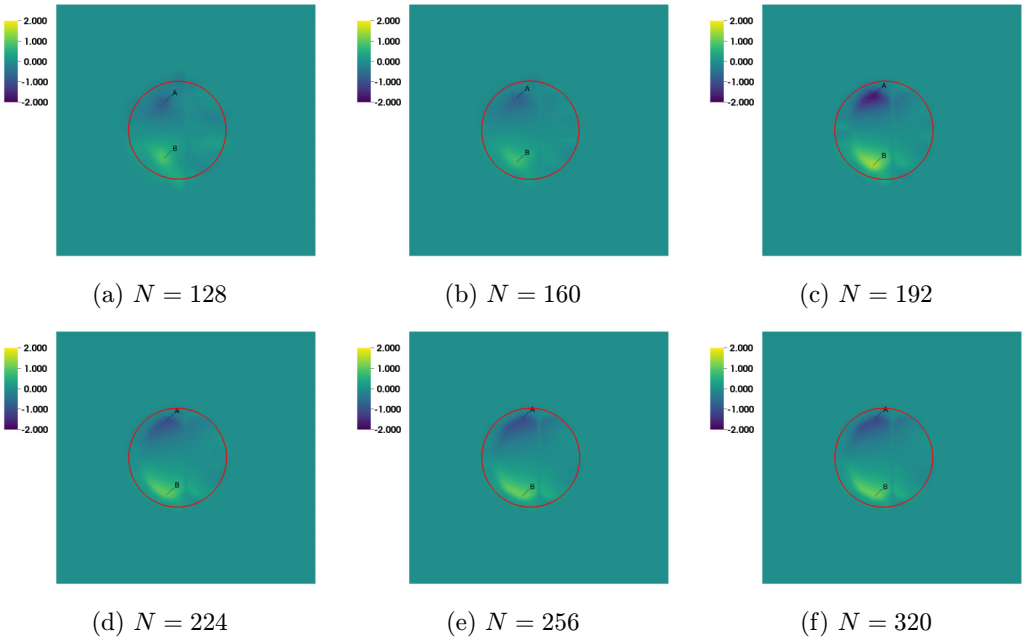

(a) $N = 128$ (b) $N = 160$ (c) $N = 192$

(d) $N = 224$ (e) $N = 256$ (f) $N = 320$

FIG. 5. (a)–(f) Pseudocolor images of the nondimensionalized magnitude of the z-component vorticity; "A" and "B" denote the maximum values of the vorticity (the definition of nondimensionalization is given in the caption of Fig. 12), and the red circle is the liquid-gas interface.

core vortex dynamics and the boundary layer dynamics contributes to the nonmonotonic behavior of the internal circulation strength and drag coefficients observed in Fig. 4. As the mesh resolution increases, the location of the largest vorticity moves closer to the boundary. It appears that for $N = 128$, the location of the largest vorticity is very close to the center of the top and bottom semispheres of the droplet. However, the core vortex region (deep blue and bright yellow parts) spreads from a very compact region at $N = 128$ to an arclike structure at $N = 320$. As the high-speed circulating fluid from the vortex moves closer to the surface, the liquid boundary layer at the liquid-gas interface must become thinner. This causes a competing action: The vortex core is better resolved as it moves, while the boundary layer is more poorly resolved. However, with sufficiently fine mesh resolution the vortex structure no longer changes, and the boundary layer can be resolved. It is interesting to note that these dynamics also affect the shapes of the droplets. For $N = 128$ and $N = 192$, the curvature of the interface on the top-left and bottom-left parts are flatter than for $N = 160$. For $N = 224$, 256, and 320, their shapes do not alter too much. In the end, both the vortex structures and the droplet shapes of $N = 256$ and $N = 320$ are almost identical, which suggests using $N = 256$.

B. Changing We at fixed ρ^*

To examine how droplet deformation will affect droplet dynamics at high pressure, we compare the droplet drag coefficient with different We at fixed $\rho^* = 20$. We first examine whether the spheroidal deformation assumption is valid or not by comparing the droplet aspect ratio with values given in the literature. Figure 6 illustrates the droplet shape under different Weber number conditions. It is clear that for We $= 3$ and We $= 6$, droplets are still close to spheroidal shape, but for We $= 9$ the droplet becomes too flat.

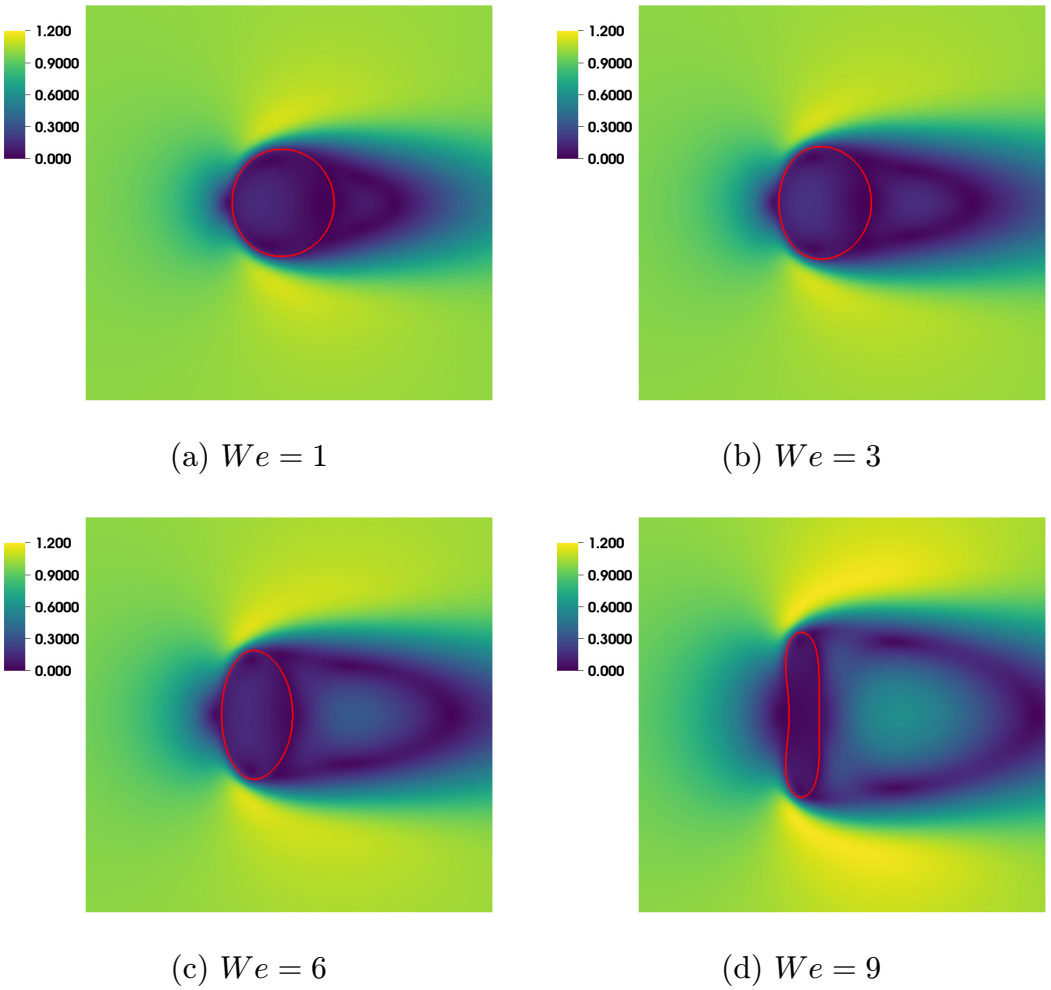

FIG. 6. (a)–(d) Droplet deformation at different We at $t^* = 10$; the pseudocolor shows the velocity magnitude normalized by inflow velocity, and the red curve is the liquid-gas interface.

1. Aspect ratio

In Ref. [14], the correlation of the aspect ratio with We, Oh, ρ^*, and μ^* was obtained through fully resolved simulations, while in Ref. [4], the correlation was found to be dependent on We only based on experimental data obtained by Reinhart [11]. The comparison is summarized in Table II,

TABLE II. Aspect ratio for different We at $\rho^* = 20$, and comparisons with Refs. [4,14].

We	1	3	6	9
e in our simulations	0.9110	0.8007	0.5869	0.1743
e in Ref. [14]	0.8910	0.7336	0.5332	0.3530
e in Ref. [4]	0.9178	0.7611	0.5662	0.4320
Error, our e compared with Ref. [14] (%)	2.253	9.157	10.07	50.64
Error, our e compared with Ref. [4] (%)	0.741	5.204	3.652	59.66

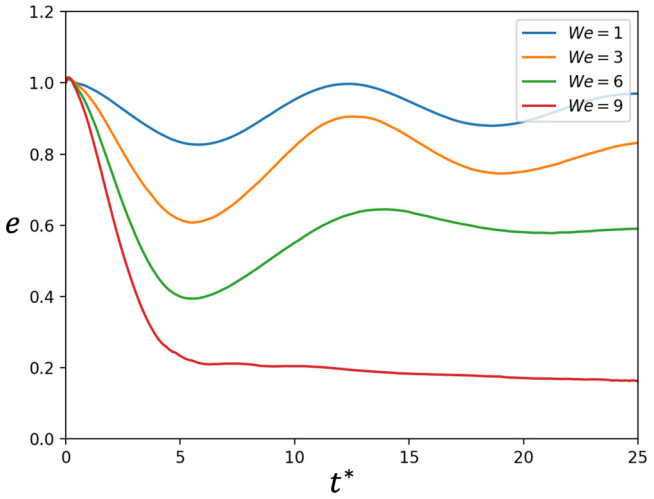

FIG. 7. The evolution of the droplet aspect ratio over time; t^* is time normalized by the capillary time scale τ_c.

and it can be found that our results have good agreement with Refs. [4,14], except for when We = 9, which is near the onset of breakup and the deformation.

The deformation has shown an oscillatory behavior; see Fig. 7. The periods of oscillation are 12.5, 12.9, and 13.5 for We = 1, 2, and 6, respectively, which are close to the theoretical prediction of 12.3 regardless of We in Ref. [35]. However, for We = 9, the deformation is so strong that oscillation did not happen.

2. Acceleration

In Fig. 8, we compare results from different acceleration calculations using drag coefficients estimated using Eq. (15). The area A_p is calculated by using e, as explained in the next section. When the droplet reaches a steady state, the results with and without acceleration are very close to each other. Their lines are parallel to each other, but deviate by a small value because of the slow motion of the droplet. During the transient period, drag coefficients calculated with acceleration are smaller than nonaccelerating cases. Acceleration calculated by $a_2 = \frac{d^2X_d}{dt^2}$ oscillates very frequently when the droplet enters from the transient state into the steady state. For acceleration calculated by $a_3 = \frac{dU_d^2}{2dX_d}$, the result performs poorly in the transient period, because a becomes too sensitive to dX_d. The back-and-forth motion of the droplet due to the gravity update scheme makes it not a good option for calculating acceleration. Therefore $a_1 = \frac{dU_d}{dt}$ is adopted in Eq. (15) and will be used for the rest of this paper.

3. Overall drag coefficient prediction

Drag coefficients calculated from Eqs. (14) and (15) are plotted in Figs. 9 and 10, respectively. In Fig. 9, the droplets are assumed to be steady, and C_d computed from different estimations of A_p are presented. One of the ways to estimate A_p is to use r_{eff}, and the other is to use the aspect ratio e to update a more accurate value of the frontal area and use that instead in the area definition. C_d computed by using r_{eff} increases with increasing We, but this trend is mild when C_d is computed by using e. In Fig. 10, the transient behavior of droplets is considered. The transient C_d in the transient time drops faster than the C_d computed using Eq. (14).

In addition, a comparison of the drag coefficient found here with the literature has been made, shown in Fig. 11. There are two sets of data for the study by Helenbrook and Edwards [14]. For

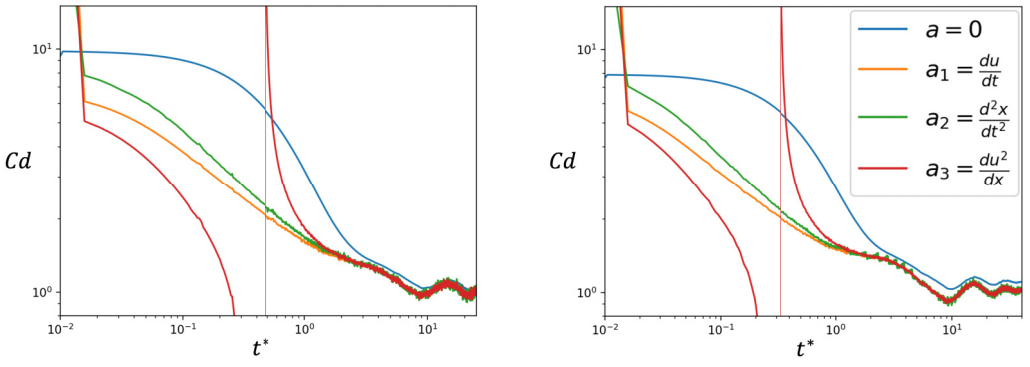

(a) $We = 1$ (b) $We = 3$

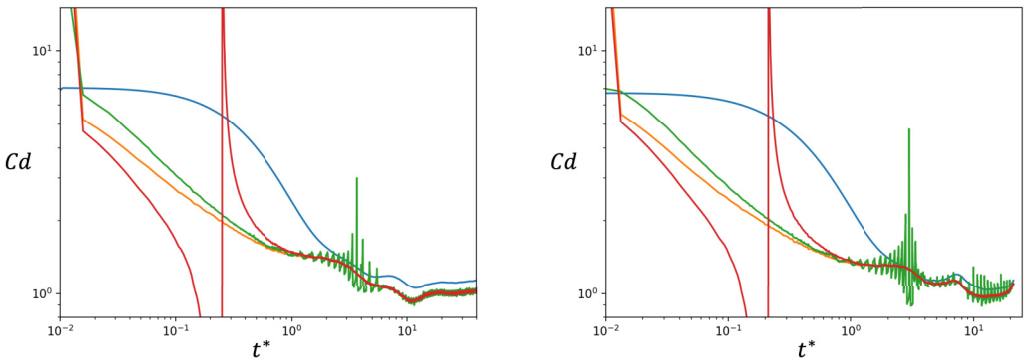

(c) $We = 6$ (d) $We = 9$

FIG. 8. (a)–(d) Drag coefficient development for different We with a calculated in different ways.

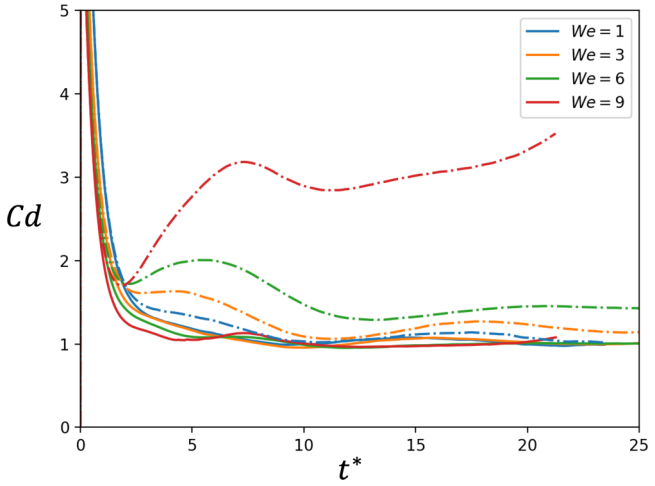

FIG. 9. Drag coefficient calculated using Eq. (14) with A_p estimated using r_{eff} (dash-dotted lines) and e (solid lines).

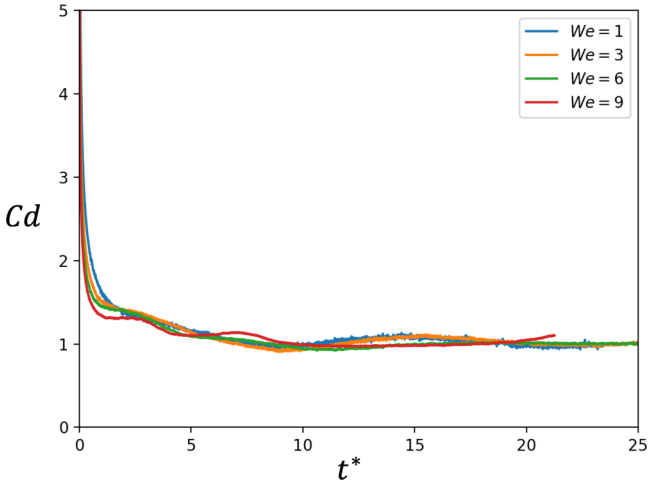

FIG. 10. Drag coefficient calculated using Eq. (15) with A_p estimated using e.

the green upward-triangle data points, C_d and e are both obtained using correlations in Ref. [14]. For the green downward-triangle data points, e is replaced by our simulation results. Blue diamond and blue square data points are from correlations in Refs. [4,12] for deformable liquid droplets, while the circle data points are only for spherical liquid droplets from Refs. [8–10]. The work of Helenbrook and Edwards considers both deformation and internal circulation. All drag coefficient correlations from the literature use r_{eff} to calculate C_d; thus we use the drag coefficient calculated using Eq. (14) for comparison.

In Fig. 11, we see that our data at low We are quite close to others' work. However, at We = 9, since the droplet is highly deformed, the shape of the droplet cannot be treated as spheroid. As a result, the evaluation of e is not accurate. Besides, results from the literature have no agreement at We = 9, meaning that predictions of C_d in the current literature perform badly when the droplet is highly deformed and near breakup.

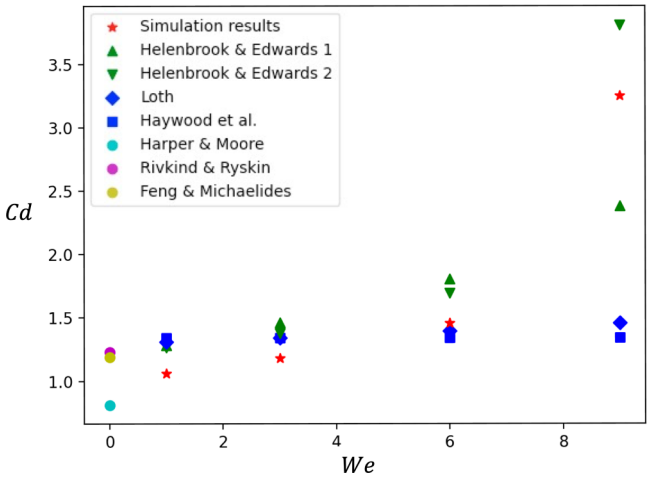

FIG. 11. Comparison of the drag coefficient found here with the literature: Helenbrook and Edwards [14], Loth [4], Haywood *et al.* [12], Harper and Moore [8], Rivkind and Ryskin [9], and Feng and Michaelides [10].

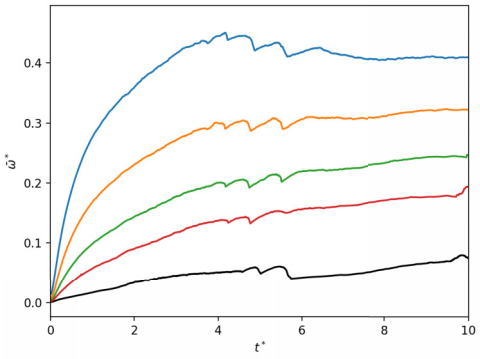

(a) $\bar{\omega}^*$ vs t^*

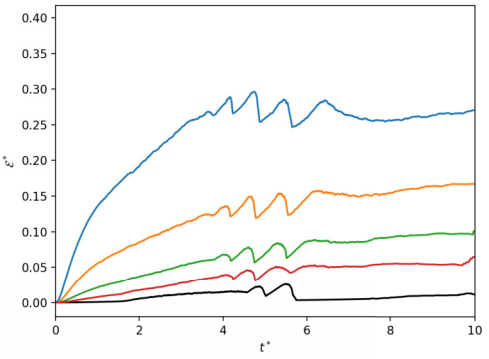

(b) $\bar{\mathcal{E}}^*$ vs t^*

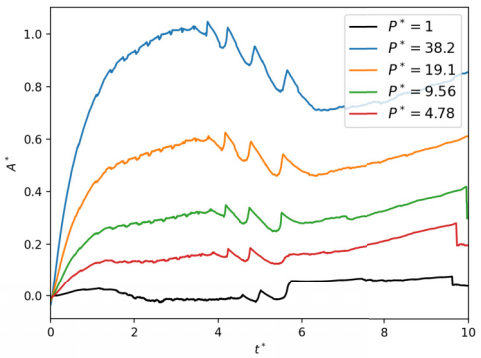

(c) $\bar{A}^*$ vs t^*

FIG. 12. Correlation between droplet internal circulation and pressure; the volume-averaged (a) vorticity, (b) enstrophy, and (c) Hill's constant are nondimensionalized by $\bar{\omega}^* = \bar{\omega}/(U_{in}/D)$, $\bar{\mathcal{E}}^* = \bar{\mathcal{E}}/(0.5(U_{in}/D)^2)$, and $\bar{A}^* = \bar{A}/(U_{in}/D^2)$.

C. Changing ρ^* at fixed We

ρ^* is the quantification of internal circulation strength [28] and is correlated to pressure through the ideal law, indicating the coupling between liquid and gas phases. This correlation can be found in Fig. 12. With increasing P^*, i.e., decreasing ρ^*, the internal circulating will become stronger regardless of the method used for measuring internal circulation strength.

To consider solely the effect of internal circulation, we compare drag coefficients at different ρ^* at fixed We $= 6$. Streamlines of droplet internal flow at We $= 6$ have been shown in Fig. 13. Strong circulation can be observed within the droplet. For droplets with very high liquid-density-to-gas-density ratio, a secondary vortex can be found at the rear of the droplet. Since the secondary vortex circulates in the orientation opposite to the primary vortex, it reduces the overall internal circulation strength [36]. The evolution of the droplet shape is shown in Fig. 14. The onset of oscillation of deformation has been observed to have slight phase shift due to the internal circulation difference in each case [37].

The steady-state drag coefficients with different ρ^* are plotted in Fig. 15. As in Sec. IV B, the C_d estimated using different A_p are presented. A clear trend is shown in the figure that decreasing the density ratio corresponds to a larger drag coefficient. This indicates that the

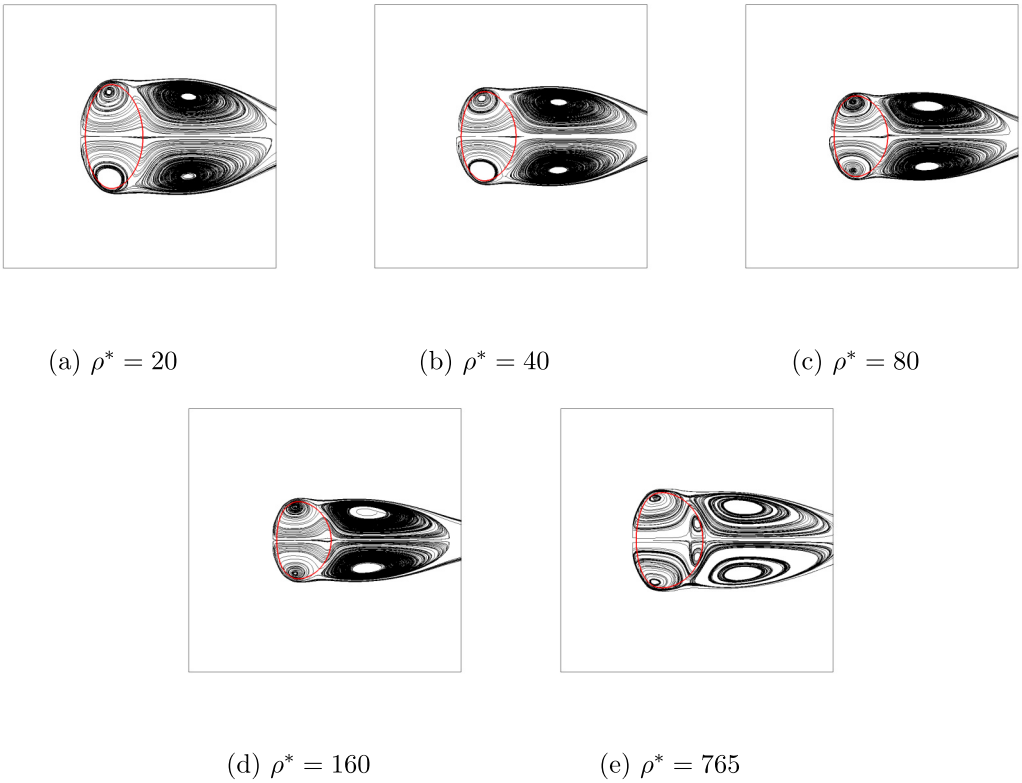

(a) $\rho^* = 20$ (b) $\rho^* = 40$ (c) $\rho^* = 80$

(d) $\rho^* = 160$ (e) $\rho^* = 765$

FIG. 13. (a)–(e) Streamlines around and inside the droplet at We $= 6$ and $t^* = 10$ with different ρ^*.

enhanced liquid and gas coupling due to high pressure will increase the drag coefficient, although it is noted that with corrected computation of A_p, the variation of C_d becomes more mild.

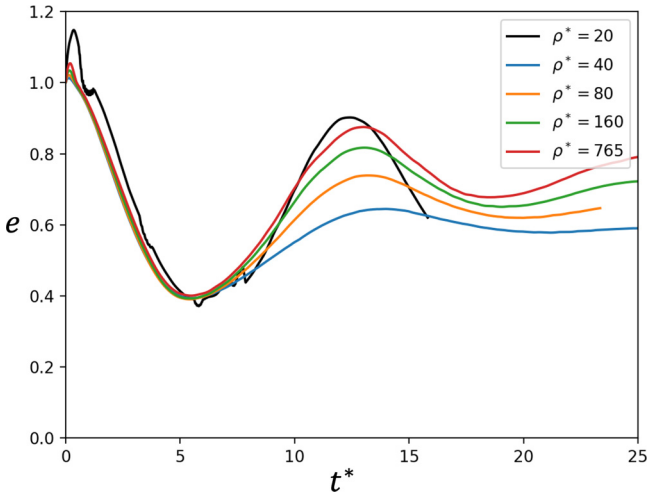

FIG. 14. The evolution of the droplet aspect ratio over time.

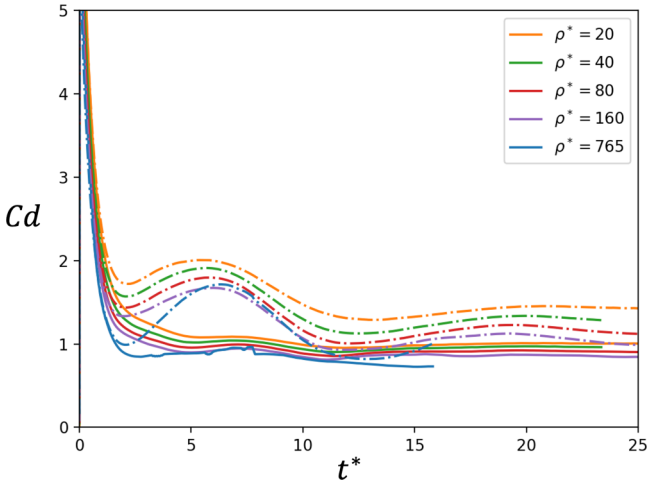

FIG. 15. Drag coefficient calculated using Eq. (14) with A_p estimated using r_{eff} (dash-dotted lines) and e (solid lines).

D. Scaling analysis of the droplet aspect ratio

We are concerned with which parameters affect the deformation of a droplet in a uniform convective flow for small-Weber-number cases. Some assumptions are made to simplify the problem. Firstly, the Ohnesorge number (Oh) is smaller than 0.1 in the case we are considering. Thus the viscous effect can be neglected [20]. Secondly, the deformed droplet is a spheroid. More specifically, it is an oblate spheroid.

For a spherical droplet, due to the shear force on the droplet interface, there will be internal circulation inside the droplet. Therefore we assume that the gas inertial energy $E_{i,g}$ will be converted into the inertial energy of the liquid, $E_{i,l}$, and also provide the energy change in the surface energy E_γ:

$$E_{i,g} \sim E_{i,l} + E_\gamma. \tag{19}$$

The initial spherical droplet has a diameter D, and after the deformation, it becomes a spheroid with semi-major-axis and semi-minor-axis lengths R_y and R_x, respectively. The aspect ratio is then calculated as $e = R_x/R_y$, which will be smaller than 1 in our case. Schematics of the spherical and deformed droplets are drawn in Fig. 3.

The inertial energies of the gas and liquid are

$$E_{i,g} \sim \tfrac{1}{2}\rho_g U_{in}^2 V, \tag{20}$$

$$E_{i,l} \sim \tfrac{1}{2}\rho_l U_s^2 V, \tag{21}$$

where U_s is the liquid velocity at the droplet surface. From the definition of e and conservation of mass, the relation between D and R_x can be found:

$$e = \frac{R_x}{R_y} \Rightarrow R_y^2 = \frac{R_x^2}{e^2}, \tag{22}$$

$$V = \frac{4}{3}\pi R_x R_y^2 = \frac{1}{6}\pi D^2 \Rightarrow R_x = \frac{1}{2} D \cdot e^{2/3}. \tag{23}$$

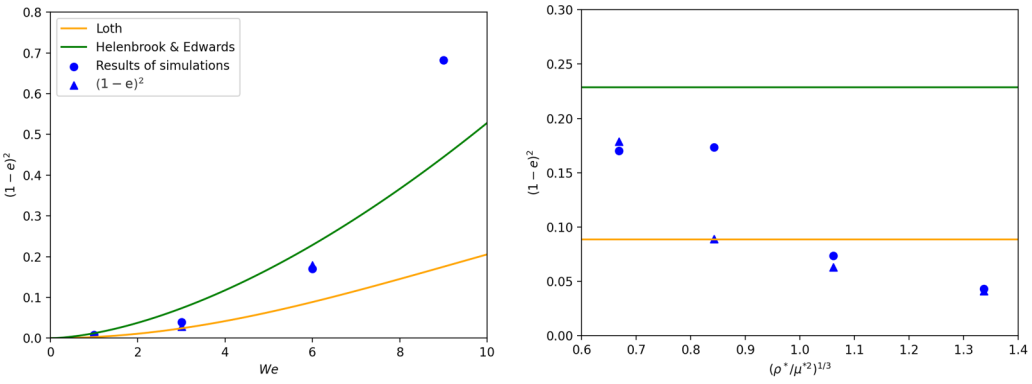

FIG. 16. Aspect ratio correlation comparison; results shown with the blue triangles were calculated using Eq. (31). (a) Aspect ratio correlation with ρ^*/μ^{*2} fixed. (b) Aspect ratio correlation with We fixed.

The surface energy change is the difference in the surface energy between the spherical and spheroidal shapes:

$$E_\gamma = \gamma(A_{\text{spheroid}} - A_{\text{sphere}}), \tag{24}$$

where $A_{\text{spheroid}} = 2\pi R_y^2 + \pi \frac{R_x^2}{\alpha} \ln(\frac{1+\alpha}{1-\alpha})$ with $\alpha = 1 - e^2$.

Usually, the freestream velocity U_{in} is known, but the droplet surface velocity U_s is unknown. To establish a correlation between U_{in} and U_s, the scaling analysis based on the continuity of shear stress at the phase interface in Ref. [13] for spherical droplets gives

$$\frac{U_s}{U_{in}} = (\rho^*\mu^*)^{-1/3}. \tag{25}$$

Using the above equations and relations, the correlation between the Weber number and the aspect ratio can be found:

$$\text{We} \cdot [1 - (\rho^*/\mu^{*2})^{1/3}] \sim 2(e^{-2/3} - 2) + \frac{e^{4/3}}{\sqrt{1-e^2}} \ln\left(\left(\frac{1+\sqrt{1-e^2}}{e}\right)^2\right). \tag{26}$$

If the deformation is very small, we can further simplify Eq. (26) by using Taylor expansion on the right-hand side at $e = 1$ and eliminating higher-order terms to get

$$(1-e)^2 \sim \text{We} \cdot (1 - (\rho^*/\mu^{*2})^{1/3}). \tag{27}$$

Equation (27) has a very limited application, because from the observation in our numerical works, the spheroidal assumption can only hold at the range around $0.5 < e < 1$.

We used data obtained from our numerical simulations by using the in-house code, together with the aspect ratio calculated from correlations in Eq. (28) from Ref. [4] and Eq. (29) from Ref. [14], to verify Eq. (27). The comparison is shown in Fig. 16(a), and ρ^*/μ^{*2} is fixed at around 0.3 for the simulations. The data point that resulted from our simulations at $\text{We}(1 - \rho^*/\mu^{*2})^{1/3} \approx 3$, which corresponds to $\text{We} = 9$, is incorrect. The highly deformed droplets cause the spheroidal assumption to fail, as can be seen in Fig. 13(e). The correlations in both Ref. [4] and Ref. [14] are dependent on the Weber number only. In Ref. [14], there is an aspect ratio correlation dependent on ρ^*/μ^{*2}, but it is only used for prolate droplets. Furthermore, it was developed in cases where the liquid-density-to-gas-density ratio is high and the viscosity ratio is small. In addition, Helenbrook and Edwards [14] and Feng and Michaelides [10] have both argued that the effect of ρ^*/μ^{*2} is minimal when the density ratio is small. In our simulations, only droplets with oblate shape were observed, and

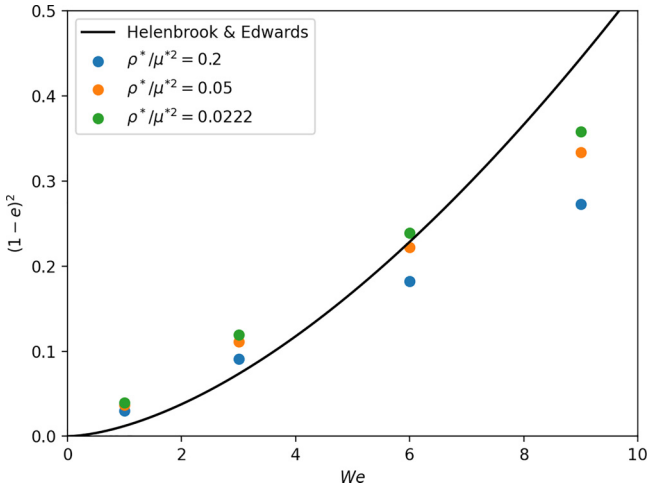

FIG. 17. Aspect ratio variation with respect to ρ^*/μ^{*2} using correlation Eq. (30).

a significant variation of the aspect ratio was found for a larger liquid-density-to-gas-density ratio, as can be seen in Fig. 16(b), where the Weber number was fixed at We = 6 and the viscosity ratio was fixed at around $\mu^* \approx 8.18$. When the density ratio is equal to 20 or 40, the aspect ratio varies very little. For a density ratio equal to 80 or 160, the aspect ratio decreases significantly. This is reasonable because when the ambient pressure is not very high, the droplet will couple less to the gas, so it will be less deformed.

$$e = 1 - 0.75 \tanh(0.07\mathrm{We}), \tag{28}$$

$$e = 1 - 0.11\mathrm{We}^{0.82}. \tag{29}$$

Figure 16 indicates that Eq. (26) is able to provide a simple correlation between We, ρ^*/μ^{*2}, and e from a physics perspective. However, since the derivation is not very rigorous, it can only be used to estimate the order of magnitude of e. Also, the use of the correlation is limited to a relatively low Weber number to exclude the severe deformation situation. Therefore we further fitted our data to find coefficients for Eq. (26) to find a more accurate correlation, Eq. (31) below. The results of the fitted correlation are compared in Fig. 16 as well. However, since the right-hand side of Eq. (26) is a concave-up curve with respect to e, it will have no solutions when the Weber number is too high or ρ^*/μ^{*2} is too small. That is why we do not have the result at We = 9 of Eq. (26) in Fig. 16(a). An alternative correlation is to fit Eq. (27), but it has lower accuracy, and the resulting correlation is Eq. (30). We substituted values of ρ^*/μ^{*2} used in Ref. [14] into the correlation to see the variation of the aspect ratio, shown in Fig. 17. When the density ratio is small, the aspect ratio does not vary too much. For a larger density ratio, the variation of the aspect ratio is obvious. The variation also becomes larger with increasing Weber number.

$$(1-e)^2 = 0.0485\mathrm{We} - 0.0311\mathrm{We}(\rho^*/\mu^{*2})^{1/3}, \tag{30}$$

$$\begin{aligned} &-0.0266\mathrm{We}\cdot(1 - 0.408(\rho^*/\mu^{*2})^{1/3}) \\ &= (1.14e^{-2/3} - 3.11) + \frac{e^{4/3}}{\sqrt{1-e^2}} \ln\left(\left(\frac{1+\sqrt{1-e^2}}{e}\right)^2\right). \end{aligned} \tag{31}$$

V. CONCLUSIONS

In this paper, we investigate the effect of deformation and internal circulation on the droplet drag coefficient in a high-pressure environment. We assume the drag coefficient to be a function of the Weber number and liquid-density-to-gas-density ratio, because they reflect the droplet deformation and internal circulation, respectively. When calculating the droplet drag coefficient, two kinds of estimations are made on the projected frontal area. The first way is to approximate the deformed droplet as an equal-volume sphere, as many studies in the literature do, and the second way is to assume that the shape of the deformed droplet is spheroid. The second way will fail when the droplet is highly deformed and about to break up. The gravity update scheme from Refs. [28,29] should force the droplet to be steady, but a transient period still exists at the early stage of development. We applied different calculation procedures for the transient acceleration of the droplet. We found that the acceleration calculated by the time derivative of the velocity was better than the acceleration calculated by the second-order time derivative of the droplet displacement, the latter oscillating frequently when turning from the transient period to the steady period due to the gravity update scheme. The droplet drag coefficient is found to be larger with increasing Weber number, i.e., stronger deformation, although when the aspect ratio is included in the definition of the area, this effect becomes very weak. In addition, with decreasing liquid-density-to-gas-density ratio corresponding to stronger internal circulation, the drag coefficient increases. However, it should be noted that deformation and internal circulation are not totally independent of each other, because when the droplet is fixed, it still has different aspect ratios with varying density ratio. An analytical expression is derived which helps explain some of the results. We further explored parameter dependencies of the aspect ratio and found that it is correlated with both the Weber number and ρ^*/μ^{*2}.

ACKNOWLEDGMENT

The authors acknowledge Advanced Research Computing at Virginia Tech for providing computational resources and technical support that have contributed to the results reported within this paper, see Ref. [38].

[1] J. A. Palmore and Y. Lin, Interface-capturing numerical studies of multicomponent spray and droplet vaporization, in *AIAA SciTech 2022 Forum* (American Institute of Aeronautics and Astronautics, Reston, VA, 2022).

[2] M. Herrmann, Detailed numerical simulations of the primary atomization of a turbulent liquid jet in crossflow, J. Eng. Gas Turbines Power **132**, 061506 (2010).

[3] J. Wen, Y. Hu, A. Nakanishi, and R. Kurose, Atomization and evaporation process of liquid fuel jets in crossflows: A numerical study using Eulerian/Lagrangian method, Int. J. Multiphase Flow **129**, 103331 (2020).

[4] E. Loth, Quasi-steady shape and drag of deformable bubbles and drops, Int. J. Multiphase Flow **34**, 523 (2008).

[5] J. Palmore, Jr., On the vaporization rate and flame shape of nonspherical droplets, J. Heat Transfer **144**, 061301 (2022).

[6] M. Setiya and J. Palmore, Jr., Evaporation of deformable liquid fuel droplets using direct numerical simulation, arXiv:2208.08479 [physics.flu-dyn].

[7] W. R. A. Goossens, Review of the empirical correlations for the drag coefficient of rigid spheres, Powder Technol. **352**, 350 (2019).

[8] J. F. Harper and D. W. Moore, The motion of a spherical liquid drop at high Reynolds number, J. Fluid Mech. **32**, 367 (1968).

[9] V. Y. Rivkind and G. M. Ryskin, Flow structure in motion of a spherical drop in a fluid medium at intermediate Reynolds numbers, Fluid Dyn. **11**, 5 (1976).
[10] Z.-G. Feng and E. E. Michaelides, Drag coefficients of viscous spheres at intermediate and high Reynolds numbers, J. Fluids Eng. **123**, 841 (2001).
[11] A. Reinhart, Das Verhalten fallender Tropfen, Chem. Ing. Tech. **36**, 740 (1964).
[12] R. J. Haywood, M. Renksizbulut, and G. D. Raithby, Numerical solution of deforming evaporating droplets at intermediate Reynolds numbers, Numer. Heat Transfer Part A **26**, 253 (1994).
[13] C. K. Law, S. Prakash, and W. A. Sirignano, Theory of convective, transient, multicomponent droplet vaporization, Symp. (Int.) Combust. **16**, 605 (1977).
[14] B. T. Helenbrook and C. F. Edwards, Quasi-steady deformation and drag of uncontaminated liquid drops, Int. J. Multiphase Flow **28**, 1631 (2002).
[15] J. Q. Feng, A deformable liquid drop falling through a quiescent gas at terminal velocity, J. Fluid Mech. **658**, 438 (2010).
[16] S. Temkin and S. S. Kim, Droplet motion induced by weak shock waves, J. Fluid Mech. **96**, 133 (1980).
[17] S. Temkin and H. K. Mehta, Droplet drag in an accelerating and decelerating flow, J. Fluid Mech. **116**, 297 (1982).
[18] Q. Qu, P. Ma, P. Liu, S. Li, and R. K. Agarwal, Numerical study of transient deformation and drag characteristics of a decelerating droplet, AIAA J. **54**, 490 (2016).
[19] J. Palmore, Jr. and O. Desjardins, A volume of fluid framework for interface-resolved simulations of vaporizing liquid-gas flows, J. Comput. Phys. **399**, 108954 (2019).
[20] D. R. Guildenbecher, C. López-Rivera, and P. E. Sojka, Secondary atomization, Exp. Fluids **46**, 371 (2009).
[21] R. Suryaprakash and G. Tomar, Secondary breakup of drops, J. Indian Inst. Sci. **99**, 77 (2019).
[22] The Engineering ToolBox, Air - Dynamic and Kinematic Viscosity, 2003, https://www.engineeringtoolbox.com/air-absolute-kinematic-viscosity-d_601.html.
[23] *NIST Chemistry WebBook*, NIST Standard Reference Database No. 69, edited by P. J. Linstrom, and W. G. Mallard (National Institute of Standards and Technology, Gaithersburg, MD, 2022).
[24] O. Desjardins, G. Blanquart, G. Balarac, and H. Pitsch, High order conservative finite difference scheme for variable density low Mach number turbulent flows, J. Comput. Phys. **227**, 7125 (2008).
[25] X.-D. Liu, R. P. Fedkiw, and M. Kang, A boundary condition capturing method for Poisson's equation on irregular domains, J. Comput. Phys. **160**, 151 (2000).
[26] M. Owkes and O. Desjardins, A computational framework for conservative, three-dimensional, unsplit, geometric transport with application to the volume-of-fluid (VOF) method, J. Comput. Phys. **270**, 587 (2014).
[27] J. A. Palmore and O. Desjardins, Validating a numerical framework for resolved simulations of vaporizing droplets, in *14th Triennial International Conference on Liquid Atomization and Spray Systems* (ILASS International, Chicago, IL, 2018), http://hdl.handle.net/10919/108312.
[28] Y. Lin, M. Setiya, and J. A. Palmore, A numerical strategy for investigating internal circulation in droplets, in *AIAA SciTech 2022 Forum* (American Institute of Aeronautics and Astronautics, Reston, VA, 2022).
[29] M. Setiya and J. Palmore, Method to study effect of straining flow on droplet vaporization at low Reynolds number, in *2020 Spring Technical Meeting of the Eastern States Section* (Combustion Institute, Pittsburgh, PA, 2020), http://hdl.handle.net/10919/108308.
[30] R. L. Panton, *Incompressible Flow* (Wiley, Hoboken, NJ, 2013).
[31] G. K. Batchelor, *An Introduction to Fluid Dynamics* (Cambridge University Press, Cambridge, 2000).
[32] T. D. Aslam, A partial differential equation approach to multidimensional extrapolation, J. Comput. Phys. **193**, 349 (2004).
[33] C. T. Crowe, J. D. Schwarzkopf, M. Sommerfeld, Y. Tsuji, J. D. Schwarzkopf, M. Sommerfeld, and Y. Tsuji, *Multiphase Flows with Droplets and Particles* (CRC, Boca Raton, FL, 2011).
[34] M. R. Maxey and J. J. Riley, Equation of motion for a small rigid sphere in a nonuniform flow, Phys. Fluids **26**, 883 (1983).
[35] N. Ashgriz, *Handbook of Atomization and Sprays: Theory and Applications* (Springer, New York, 2011).

[36] P. S. Ayyaswamy, S. S. Sadhal, and L. J. Huang, Effect of internal circulation on the transport to a moving drop, Int. Commun. Heat Mass Transfer **17**, 689 (1990).
[37] F. Mashayek and N. Ashgriz, Nonlinear oscillations of drops with internal circulation, Phys. Fluids **10**, 1071 (1998).
[38] https://arc.vt.edu/.